9-9-2020

A Statistical Impulse Response Model Based on Empirical Characterization of Wireless Underground Channel

Abdul Salam
Purdue University, salama@purdue.edu

Mehmet C. Vuran

Suat Irmak

A Statistical Impulse Response Model Based on Empirical Characterization of Wireless Underground Channels

Abdul Salam, *Member, IEEE*, Mehmet C. Vuran, *Member, IEEE*, and Suat Irmak

***Abstract*— Wireless underground sensor networks (WUSNs) are becoming ubiquitous in many areas. The design of robust systems requires an extensive understanding of the underground (UG) channel characteristics. In this article, the UG channel impulse response is modeled and validated via extensive experiments in indoor and field testbed settings. Three distinct types of soils are selected with sand contents ranging from 13% to 86%, and clay contents ranging from 3% to 32%. The impacts of changes in soil texture and soil moisture are investigated with more than 1,200 measurements in a novel UG testbed at the University of Nebraska-Lincoln that allows flexibility in soil moisture control. Moreover, the time-domain characteristics of the channel, such as the RMS delay spread, coherence bandwidth, and multipath power gain, are analyzed. The power delay profile analysis validates the three main components of the UG channel: direct, reflected, and lateral waves. Furthermore, it is shown that the RMS delay spread follows a log-normal distribution. The coherence bandwidth ranges between 650 kHz and 1.15 MHz for soil paths of up to 1 m and decreases to 418 kHz for distances above 10 m. Soil moisture is shown to affect the RMS delay spread non-linearly, which provides opportunities for soil moisture-based dynamic adaptation techniques. A statistical channel model for the wireless underground channel has been developed based on the measurements and analysis. The statistical model shows good agreement with the measurement data. The model and analysis pave the way for tailored solutions for data harvesting, UG sub-carrier communication, and UG beamforming.**

Manuscript received April 14, 2019; revised January 25, 2020 and April 21, 2020; accepted May 27, 2020. Date of publication June 5, 2020; date of current version September 10, 2020. This work was supported in part by NSF Grants under Grant NSF CNS-1619285, Grant DBI-1331895, and Grant NSF CNS-1423379; in part by the NSF CAREER Award under Grant CNS-0953900 and Grant NSF CNS-1247941; and in part by the NSF Cyber-Innovation for Sustainability Science and Engineering (CyberSEES) under Grant DBI-1331895. The article was presented in part at the Proceedings of the 35th IEEE International Conference on Computer Communications (IEEE INFOCOM 2016), San Francisco, USA, April 2016 and in part at the 14th IEEE International Conference on Networking, Sensing, and Control (IEEE ICNSC), Calabria, Italy, May 2017. The associate editor coordinating the review of this article and approving it for publication was D. Matolak. *(Corresponding author: Abdul Salam.)*

Abdul Salam is with the Department of Computer and Information Technology, Purdue University, West Lafayette, IN 47907 USA (e-mail: salama@purdue.edu).

Mehmet C. Vuran is with the Cyber-Physical Networking Laboratory, Department of Computer Science and Engineering, University of Nebraska–Lincoln, Lincoln, NE 68588 USA (e-mail: mcv@unl.edu).

Suat Irmak is with the Department of Biological Systems Engineering, University of Nebraska–Lincoln, Lincoln, NE 68588 USA (e-mail: sirmak2@unl.edu).

Color versions of one or more of the figures in this article are available online at http://ieeexplore.ieee.org.

Digital Object Identifier 10.1109/TWC.2020.2998762

***Index Terms*— Cyber-physical systems, underground electromagnetic propagation, wireless underground sensor networks, precision agriculture.**

I. Introduction

WIRELESS underground sensor networks (WUSNs) are becoming ubiquitous in many areas including precision agriculture [1], [2], [13], [26]–[29], [31], [41], environment and infrastructure monitoring [3], [15], [22], [36], [38], and border patrol [5]. The establishment of robust wireless underground communication links between two underground nodes (UG2UG link) or between an underground node and a node above the surface (UG2AG link) requires analysis of the underground (UG) channel characteristics.

In general, multipath fading degrades the performance of a communication channel [16]. Moreover, the UG communication channel is affected by multipath fading caused by reflection and refraction of electromagnetic (EM) waves in soil and at the soil-air interface. A detailed characterization of the UG channel is required to reduce the effects of these disturbances. Traditional over-the-air (OTA) communication channel models cannot be readily used in WUSNs because EM waves in soil suffer higher attenuation than in air due to their incidence in lossy media which consists of soil, water, and air, and accordingly, leads to permittivity variations over time and space with changes in soil moisture [13]. WUSNs are generally deployed at depths, which are less than 50cm [8]. Due to the proximity to the Earth's surface, a part of the transmitted EM waves propagates from soil to air, then travel along with the soil-air interface, and enter the soil again to reach the receiver. These EM waves (i.e., *lateral waves* [21]) constitute a significant component of the UG channel.

EM wave propagation analysis in an underground channel is challenging because of its computation complexity [5]. In [12] and [40], channel models based on the analysis of the EM field and Friis equations have been developed and direct, reflected, and lateral waves are shown to be significant contributors of received signal strength. These models provide good approximations when coarse channel measures (e.g., path loss) are concerned but are limited due to the lack of insight into channel statistics (e.g., delay spread and coherence bandwidth) and empirical validations.

Partly unique to the UG channel, there are mainly four types of physical mechanisms that lead to variations in the UG channel statistics, the analyses of which constitute the major contributions of this article:

1) Soil Texture and Bulk Density Variations: EM waves exhibit attenuation when incident in a soil medium. These variations are a function of soil texture and bulk density. For example, sandy soil holds less bound water, which is the major component in soil that absorbs EM waves. The water holding capacity of fine-textured soils (silt loam, fine sandy loam, and silty clay loam) is higher than coarse-textured soils (sand, sandy loam, loamy sand), because of the small pore size, as compared to coarse soils. Medium textured soils have smaller pore sizes and hence, no aggregation and reduced resistance against gravity [14]. To cover a wide array of soil texture and bulk density variations, we have performed experiments in three distinct types of soil.

2) Soil Moisture Variations: The effective permittivity of soil is a complex number. Thus, besides diffusion attenuation, the EM waves also suffer from an additional attenuation caused by the absorption of soil water content. To this end, experiments are conducted with controlled soil moisture variations in an indoor testbed.

3) Distance and Depth Variations: Received signal strength varies with the depth of and distance between transmitter and receiver antennas because different components of EM waves suffer attenuation based on their travel paths. Sensors in WUSN applications are usually installed between 1 3feet soil layer, which covers most of the root growth and soil-water activities. Therefore, we have taken measurements for depths of 10 40cm with transmitter-receiver (T-R) distances of 50cm to 12m for UG2UG experiments. Near-field effects of underground antenna for frequency range used in these experiments are within the 30cm region. Besides, UG2AG experiments are conducted for radii of 2 7m with receiver angles of 0 -90 taken in the vertical plane as normal to the soil-air interface.

4) Frequency Variations: The path loss caused by the attenuation is frequency dependent [10]. Besides, when EM waves propagate in soil, their wavelength shortens due to higher permittivity of soil than the air. Channel capacity in the soil is also a function of operating frequency. Channel transfer function measurements (S_{21}) are taken to analyze the effects of frequency on underground communication.

Given the effects of these factors, the design of digital communication solutions for wireless underground channels merits a detailed characterization of the effects of these physical phenomena of soil on propagation between wireless underground channel transmitter and receiver. This requires extensive measurements to derive the model channel parameters such as the RMS delay spread, channel gains, and coherence bandwidth through empirical measurements. These parameters are useful for performance evaluation of a digital communication system operating in wireless underground channels. Therefore, it is crucial to have a realistic underground channel model. A statistical model developed from empirical observations should not only capture the effects of all the physical processes undergoing in soil but also exhibit a close match with the measurement data.

In this article, we present a UG channel impulse response model and the corresponding analysis based on measured data collected from UG channel experiments with a 250ps delay resolution. Statistical properties of multipath profiles measured in different soil types under different soil moisture levels are investigated. The results presented here describe root mean square (RMS) delay spread, distribution of the RMS delay spread, mean amplitude across all profiles for a fixed T-R displacement, effects of soil moisture on peak amplitudes of power delay profiles, mean access delay, and coherence bandwidth statistics. The goal of the measurement campaign and the corresponding model is to produce a reliable channel model which can be used for different types of soils under different conditions. Thus, we have considered several possible scenarios with more than $1\ 500$ measurements taken over a period of 10 months.

The rest of the paper is organized as follows: We provide a background on underground wireless communications in Section II. The related work is discussed in Section III. A description of the UG channel impulse response model is given in Section IV. In Section V, measurement sites and procedures are described. The results and analysis of measured impulse responses are presented in Section VI. The wireless underground channel statistical model is presented in Section VII. In Section VIII, the power delay profile measurements are presented. Finally, the paper is concluded in Section IX.

II. Background

Electromagnetic (EM) wave communication in the underground channel consists of three types of links [5], namely underground to aboveground (UG2AG), aboveground to underground (AG2UG), and underground to underground (UG2UG). The wavelength of an EM wave incident into the soil is affected by the dielectric properties of the soil. Soil texture and its water holding capacity, bulk density, and salinity affect the propagation of waves. It is important to understand the physical processes in the soil to analyze wave propagation in soil. Soil medium consists of mineral particles, pore space (voids), and water. Soil texture comprises of silt, clay, and sand. The percentage of these particles, as well as their distributions, determine soil textural classification. The complex dielectric constant of soil consists of $_{s}$ and $_{s}$. The dielectric constant of a soil, which is fully dried, is not dependent on frequency, and is given by [39]:

$$_{s} = [1 + 0\ 44\ _{b}]^2 \tag{1}$$

where $_{b}$ is the bulk density of soil. The bulk density is defined as the ratio of the dry soil mass to bulk soil volume including pore space. The dielectric spectra of the soil become more complicated with the increase in moisture content. Water content in the soil exists usually in the form of bound water, which refers to water molecules held by soil particles and depends on numerous factors, including particle size

distribution. The water content is a strong function of bound water. The amount of water in the soil can be expressed in either volumetric or gravimetric basis. While both expressions are used in different disciplines, volumetric expressions are more commonly used.

Electromagnetic waves traveling in soil interact with soil particles, air, and water. When different quantities of water molecules bound with soil particles interact with EM waves, they exhibit different dielectric dispersion characteristics. Thus, the dielectric constant depends on the frequency of EM waves. While it is called a *constant*, the dielectric is not a constant value in the soil as it changes with several factors, including soil water content. However, in general, the increase in the dielectric constant of the soil with water content does not differ significantly with soil type (particle size distribution), particularly in high-frequency applications. Thus, the dielectric constant is a useful indicator of soil water content in different soil types. In addition to the water content and frequency, other factors such as bulk density and soil texture also affect the permittivity of soil.

In [10], dielectric properties of soil are modeled for frequencies higher than $1\,4\mathrm{MHz}$. In [23], this model is modified through extensive measurements to characterize the dielectric behavior of the soil in the frequency range of $300\mathrm{MHz}$ to $1\,3\mathrm{GHz}$. Accordingly, the relative complex dielectric constant of the soil-water mixture is given as:

$$_{\mathrm{s}} = \quad _{\mathrm{s}} \quad i\epsilon_{\mathrm{s}} \tag{2}$$

which depends on the soil texture, volumetric water content, bulk density, frequency, and particle density.

III. Related Work

Wireless communication in WUSNs is an emerging field, and few models exist to represent the underground communication. In [40], we have developed a 2-wave model, but lateral waves are not considered. In [7], models have been developed, but these do not consider underground communication. A model for underground communication in mines and road tunnels has been developed in [36], but it cannot be applied to WUSN due to wave propagation differences between tunnels and soil. We have also developed a closed-form path loss model using lateral waves in [12], but channel impulse response and statistics cannot be captured through this model.

Wireless underground communication shares characteristics of underwater communication [6]. However, underwater communication based on electromagnetic waves is not feasible because of high attenuation. Therefore, alternative techniques, including acoustic [6], are used in underwater communications. The acoustic technique cannot be used in the UG channel due to vibration limitations. In magnetic induction (MI), [22], [37], the signal strength decays with inverse cube factor and high data rates are not possible. Moreover, communication cannot take place if the sender and receiver coils are perpendicular to each other. Therefore, the MI cannot be readily implemented in WUSNs.

To the best of our knowledge, this is the first measurement campaign conducted to analyze and measure the channel impulse response of UG channel and the first work that proposes guidelines for the development of a novel WUSN testbed to improve the accuracy, to reduce the time required to conduct WUSN experiments, and to allow flexibility in soil moisture control.

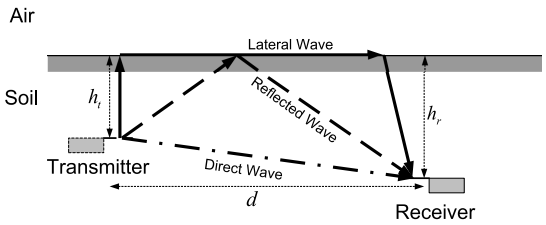

Fig. 1. The three EM waves in an underground channel [12].

IV. Impulse Response of UG channel

A wireless channel can be completely characterized by its impulse response. Traditionally, a wireless channel is modeled as a linear filter with a complex valued low pass equivalent impulse response which can be expressed as [20]:

$$\mathrm{h}(t) = \sum_{p=0}^{P\ \ 1} \quad _p \ (t \quad \ _p) \tag{3}$$

where P is the number of multipaths, and $_p$ and $_p$ are the complex gain and delay associated with path p, respectively.

A schematic view of the UG channel is shown in Fig. 1, where a transmitter and a receiver are located at a distance of d and depths of B_t and B_r, respectively [12]. Communication is mainly conducted through three EM waves: (1) The direct wave, which travels through the soil from the transmitter to the receiver, (2) the reflected wave, which also travels through the soil and is reflected from the air-soil interface, and (3) the lateral wave, which propagates out of the soil, travels along the surface and enters the soil to reach the receiver.

Based on this analysis, the UG channel process can be expressed as a sum of direct, reflected and lateral waves. Hence (3) is rewritten for UG channel as:

$$\begin{aligned}\mathrm{h_{ug}}(t) = &\sum_{i=0}^{L\ \ 1} \ _{\mathrm{l},i} \ (t \quad \ _{\mathrm{l},i}) + \sum_{j=0}^{D\ \ 1} \ _{\mathrm{d},j} \ (t \quad \ _{\mathrm{d},j}) \\ &+ \sum_{k=0}^{R\ \ 1} \ _{\mathrm{r},k} \ (t \quad \ _{\mathrm{r},k})\end{aligned} \tag{4}$$

where respectively for lateral, direct, and reflected waves; L, D, and R are the number of multipaths; $_{\mathrm{l},i}$, $_{\mathrm{d},j}$, and $_{\mathrm{r},k}$ are the complex gains; and $_{\mathrm{l},i}$, $_{\mathrm{d},j}$, and $_{\mathrm{r},k}$ are the path delays.

The received power is the area under the profile and is calculated as the sum of powers in all three components in the profile. Accordingly, the received power is given as:

$$P_{\mathrm{r}} = \sum_{i=0}^{L\ \ 1} \ _{\mathrm{l},i}\ ^2 + \sum_{j=0}^{D\ \ 1} \ _{\mathrm{d},j}\ ^2 + \sum_{k=0}^{R\ \ 1} \ _{\mathrm{r},k}\ ^2 \tag{5}$$

Then, the path loss is given as:

$$PL(\mathrm{dBm}) = P_{\mathrm{t}}(\mathrm{dBm}) + G_{\mathrm{t}}(\mathrm{dBi}) + G_{\mathrm{r}}(\mathrm{dBi}) \quad P_{\mathrm{r}}(\mathrm{dBm}) \tag{6}$$

(a) (b) (c) (d) (e)

Fig. 2. Testbed Development: (a) Testbed box, (b) Packed soil, (c) Layer of gravel at the bottom of the testbed, (d) Antenna placement, (e) Final outlook.

where P_{t} is the transmit power, P_{r} is the received power, and G_{t} and G_{r} are transmitter and receiver antenna gains, respectively. The antenna effects are included, intrinsically, in the impulse response, $\mathrm{h_{ug}}(t)$, which is obtained from the channel transfer function. Traditionally, the impulse response of an indoor wireless channel is also dependent on the antenna properties because power radiated and received in a particular direction is defined by the directive gains of transmitter and receiver antennas [25]. In our experiments and analysis, we use omni-directional dipole antennas to observe multipath components in all directions.

Next, we review the metrics derived from the channel impulse response, including excess delay and delay spread. Excess delay is defined as the time delay between the first and last arriving components. Last component is defined by a threshold value in dB relative to the strongest component in the power delay profile (PDP). Typically, a threshold value of -30dB is used [16], [25]. Mean excess delay ( ) is defined as the first moment of power delay profile and is given as [25]:

$$= \sum_{k} P_k \ _k \Big/ \sum_{k} P_k \tag{7}$$

where P_k and $_k$ are the absolute instantaneous power and the delay of the kth bin.

Root mean square (RMS) delay spread is the square root of the second central moment of the power delay profile and is given as [25]:

$$_{\mathrm{rms}} = \sqrt{\overline{^2} \quad (\overline{\ })^2} \tag{8}$$

where $\overline{^2} = \sum_{k} P_k \ ^2_k \ \sum_{k} P_k^2$, P_k is the absolute instantaneous power at k^{th} bin, and $_k$ is the delay of the k^{th} bin. The RMS delay spread is a good indicator of multipath spread and it indicates the potential of inter-symbol interference (ISI).

V. Measurement Sites and Procedures

Measurements are conducted in an indoor testbed (Section V-A) and outdoor field settings (Section V-B). The measurement procedures are explained in Section V-C.

A. Indoor Testbed

Conducting WUSN experiments in outdoor settings is challenging. These challenges include lack of availability of a wide range of soil moisture levels over a short period, the difficulty of dynamic control over soil moisture, changing soil types, and installation/replacement of equipment. Furthermore, extreme temperature effects make it hard to conduct experiments.

To overcome these challenges faced in outdoor environments, an indoor testbed is developed in a greenhouse setting using the detailed procedures described in [18], [19]. A 100 x36 x48 wooden box (Fig. 2(a)) is assembled with wooden planks that can contain up to $90\mathrm{feet}^3$ of packed soil. A drainage system is installed at the bottom, and the sides of the box are covered with a waterproof tarp to stop water seepage from sides. Before the installation of antennas and sensors, 3" layer of gravel is laid at the bottom of the box for free drainage of water (Fig. 2(b)) and then, the soil is placed in the box (Fig. 2(c)). Two PVC drainage outlets installed at the bottom of the testbed allow freely-drained (due to gravitational force only) water to exit the system. The soil profile was wetted uniformly in the entire testbed using drip lateral with drip emitters installed every $25\mathrm{cm}$ to ensure uniform wetting of the soil profile.

To monitor the soil moisture level, 8Watermark sensors are installed on each side of the box at $10\mathrm{cm}$, $20\mathrm{cm}$, $30\mathrm{cm}$ and $40\mathrm{cm}$ depths. Although in agricultural operations, environmental monitoring, and security applications; soil moisture sensors can be installed at different depths, depending on several variables, the most common maximum installation/application depth is about $4\mathrm{feet}$ from the soil surface. Depending on the purpose of the soil moisture data use, in many applications such as in shallow-rooted cropping systems, sandy soils, and numerous other applications, monitoring soil moisture in the upper soil layer (i.e., $0 \quad 60\mathrm{cm}$) can be sufficient.

These sensors are connected to two Watermark dataloggers. Soil is packed after every $30\mathrm{cm}$ by using a tamper tool to achieve a bulk density similar to real-world field conditions. This process is repeated for antenna installation at each depth. Three sets of four dipole antennas are installed (Fig. 2(d)) at the depths of $10\mathrm{cm}$, $20\mathrm{cm}$, $30\mathrm{cm}$, and $40\mathrm{cm}$. At each depth, four antennas are deployed $50\mathrm{cm}$ apart from each other. The final outlook of the testbed is shown in Fig. (e).

We conduct experiments in two different types of soils in the indoor testbed: silt loam and sandy soil. Particle size distribution and classification of testbed soils are given in Table I. To investigate the effects of soil texture on underground communication, soils selected for use in the testbed have sand contents ranging from 13% to 86% and

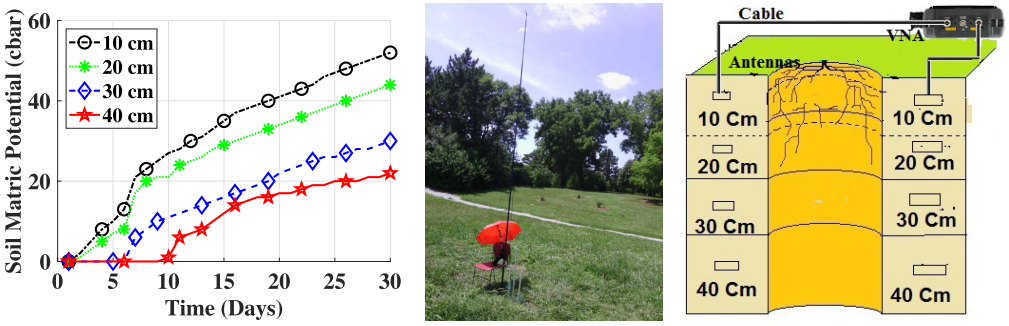

(a) (b) (c)

Fig. 3. (a) Soil moisture (expressed as soil matric potential; greater matric potential values indicate lower soil moisture and zero matric potential represents near saturation condition) with time in silt loam testbed, (b) Outdoor testbed in a field setting, (c) Experiment layout.

TABLE I
PARTICLE SIZE DISTRIBUTION AND CLASSIFICATION OF TESTBED SOILS

Textural Class	%Sand	%Silt	%Clay
Sandy Soil	86	11	3
Silt Loam	33	51	16
Silty Clay Loam	13	55	32

TABLE II
UNDERGROUND CHANNEL MEASUREMENT PARAMETERS

Parameter	Value
Start Frequency	10 MHz
Stop Frequency	4 GHz
Number of Frequency Points	401
Transmit Power	5 dBm
Vector Network Analyzer	Agilent FieldFox

clay contents ranging from 3% to 32%. Before starting the experiments, the soil is nearly saturated to attain the highest possible level of volumetric water content (VWC) and then measurements are collected as the water content is first reduced to field capacity[1] and then subsequently dried down to near wilting point.[2] The changes in soil moisture level with time are shown in Fig. 3(a) for silt loam soil.

B. Field Site

To compare with the results of indoor testbed experiments and conduct underground-to-aboveground experiments, a test-bed of dipole antennas has been prepared in an outdoor field with silty clay loam soil (Fig. 3(b)). Dipole antennas are buried in soil at a burial depth of 20cm with distances from the first antenna as 50cm-12m. A pole with adjustable height is used to conduct underground-to-aboveground (UG2AG) experiments with radii of 2m, 4m, 5 5m and 7m[3] with receiver angles of 0 , 30 , 45 , 60 , and 90 .

C. Measurement Methods

Accurate measurement of channel impulse response can be obtained from frequency domain measurements due to Fourier transform the relationship between transfer function and channel impulse response [17]. Accordingly, we have obtained channel impulse response by taking frequency-domain measurements and then taking inverse Fourier transform. A diagram of the measurement layout is shown in Fig. 3(c). The frequency response of the channel is measured using a Vector Network Analyzer (VNA). VNA-based channel measurements are popular for measuring channel transfer functions in wireless communications and antenna domains [9], [16], [17], [25], [34], [35]. The measurement parameters are given in Table II. The VNA generates a linearly swept frequency signal [24] which is propagated over a frequency range of 10MHz to 4GHz. In this range, VNA records 401 complex tones and stores them on external storage for post-processing. The discretized complex channel frequency response H_n is given by [35]:

$$\mathrm{H}_n = \mathrm{H}(f_{\text{start}} + n f_{\text{inc}}) \tag{9}$$

where f_{start} and f_{inc} are the start and increment frequencies of the sweep, respectively. The n is number of evenly spaced data points across the frequency range. H_n is obtained by measuring the reference (R) and input (A) channels and taking the complex ratio, such that $\mathrm{H}_n = \mathrm{A}_n \ \mathrm{R}_n$. This process is repeated over the frequency range F_{sweep} at n discrete points, such that $f_{\text{inc}} = F_{\text{sweep}}/n$. To obtain channel impulse response, the complex frequency data is inverse Fourier transformed. The resulting N point complex channel impulse response has a delay bin spacing of $1/F_{\text{sweep}}$ and an unambiguous FFT range of N/F_{sweep}. The measured H_n are windowed using a minimum three term Blackman-Harris window [35] because of its excellent side lobe suppression and relatively wide main lobe width. Before time domain conversion, the windowing

[1]The amount of soil-water held by soil particles after the excess water is freely drained, which takes about 2−3days.

[2]The water content level at which water is no more available to plants.

[3]The maximum distance of 7m is due to the limitations of the antenna cable length for VNA.

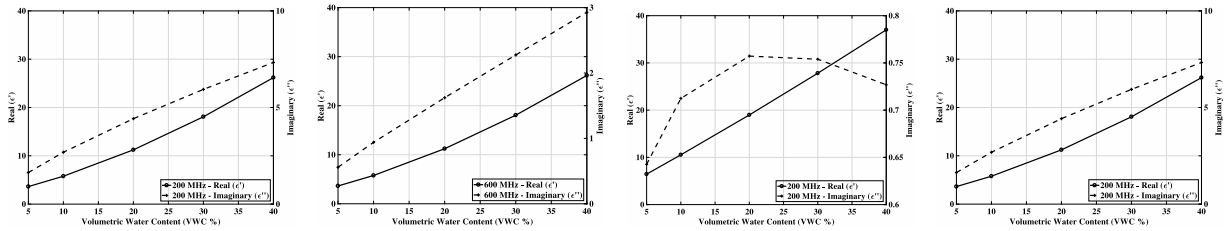

(a) Siltloam - 200 MHz (b) Siltloam - 600 MHz (c) Sandy - 200 MHz (d) Sandy - 600 MHz

Fig. 4. The dielectric constant of siltloam and sandy soil at 200MHz and 600MHz frequency.

of H_n is required to avoid sinc^2 side lobes associated with rectangular nature of frequency sweep [35].

In Figs. 4, the real and imaginary parts of dielectric constant in silt loam and sandy soil are shown for operation frequencies of $200\,\text{MHz}$ and $600\,\text{MHz}$ and water content values of 5%-60%. It can be observed that $_s$ increases linearly with the volumetric water content of the soil. Moreover, the imaginary part in Fig. 4(c) does not increase monotonically with volumetric water content. The dielectric constant of the soil depends on the many factors such as soil texture, volumetric water content, bulk density, frequency, and particle density. At low frequencies, e.g., 200MHz, in the sandy soil, the permittivity may not always be accurately predicted with the Peplinski model, because the model may not be as effective with sandy soil at lower frequencies with high sand content [23].

VI. Analysis and Results

A. Characterization of UG Channel Impulse Response

The excess delay, mean access delay (7), RMS delay spread (8) [9], [25], [34], and coherence bandwidth in relation to the RMS delay spread [17] are the parameters used to characterize the UG channel. For channel characterization, these parameters are used because system performance is not affected by the actual shape of PDP [34]. In the following, we discuss these metrics and the effects of soil moisture, soil types, distance, and depth on these metrics.

1) Statistics of Mean Excess Delay: Distribution of mean excess delay for 50cm and 1m distance over all four depths in indoor testbed (silt loam) experiment is given in Fig. 5(a). Higher mean excess delay can be observed with the increase in T-R separation, which corresponds to an increase of 2 3ns (8%). In Table III, statistics for mean ( ) and standard deviation ( ) for the mean excess delay for 50cm and 1m distances, and the 4 depths are shown. The mean excess delay increases with the depth of transmitter and receiver. In Fig. 5(b), excess delay is shown as a function of distance at 20cm depth in field (silty clay loam) experiment. It can be observed that excess delay is increased from 40ns up to 116ns as UG communication distance increases from 50cm to 12m.

2) Analysis of RMS Delay Spread: Distribution of the RMS delay spread for T-R separations of 50cm and 1m in indoor testbed (silt loam) experiment are shown in Fig. 6(a) with statistical fits. Our analysis shows that empirical distribution of $_{\text{rms}}$ follows a log-normal distribution with mean values of $23\ 94\text{ns}$ and $24\ 05\text{ns}$ and standard deviations of $3\ 7\text{ns}$ and $3\ 4\text{ns}$ for 50cm and 1m distances, respectively. In Table III, the statistics for mean ( ) and standard deviation ( ) of the RMS delay spread for T-R distances of 50m and 1m, and the four depths are shown. It can be observed from Fig. 6(a) and Table III that the RMS delay spread ($_{\text{rms}}$) increases with the burial depth for T-R distance of $1\,\text{m}$. For this case, an average increase of $3\ 68\text{ns}$ ($16\ 8\%$) is observed for the RMS delay spread when depth is increased from 10cm to 40cm. For 50cm distance, a $4\ 9\text{ns}$ increase in the mean RMS delay spread can be observed when burial depth is increased from 10cm to 20cm. This is mainly attributed to lateral waves, because at 20cm, lateral waves reach the receiver after the direct waves. At 40cm, the RMS delay spread decreases to $23\ 91\text{ns}$ because lateral waves attenuate more as the burial depth increases. In Fig. 6(b), the RMS delay spread is shown as a function of the T-R distance at 20cm depth in field (silty clay loam) experiment. It can be observed that the RMS delay spread is increased to 48ns at a distance of 12m.

The increase in the RMS delay spread with depth and distance is contributed by the strong multipath components associated with the lateral and reflected components, since their propagation time differences increase with distance. This increase in the RMS delay spread is an important result as it limits the system performance in terms of coherence bandwidth. It has been shown by analysis and simulations that the maximum data rate that can be achieved without diversity or equalization is a few percent of the inverse of the RMS delay spread [17]. Using this relationship, a coherence bandwidth is established for the RMS delay spread. For our analysis, we use 90% signal correlation ($\frac{1}{50}$ $_{\text{rms}}$) as an approximation of coherence bandwidth, because underground channel experiences higher attenuation in soil as compared to terrestrial WSNs, where typically 50% and 70% signal correlation values are used to approximate coherence bandwidth.

In Fig. 6(c), the distribution of coherence bandwidth for 50cm and 1m distance over the four depths in indoor testbed (silt loam) experiment is shown. It is observed that the range of coherence bandwidth for the UG channel is between 650kHz and $1\ 15\text{MHz}$ for distances up to 1m. In Fig. 6(d), coherence bandwidth as a function of distance in the field (silty clay loam) experiment is shown. It can be observed that the coherence bandwidth decreases to 418kHz (63%) as

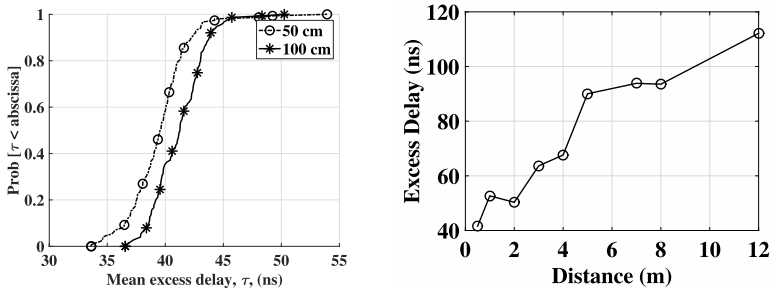

(a) (b)

Fig. 5. (a) Distribution of mean excess delay in indoor testbed (silt loam) experiment, (b) Excess delay with distance at 20cm depth in field (silty clay loam) experiment.

TABLE III

MEAN ( ) AND STANDARD DEVIATION ( ) IN NANOSECONDS FOR THE MEAN EXCESS DELAY AND THE RMS DELAY SPREAD IN INDOOR TESTBED (SILT LOAM) EXPERIMENT

Depth	Mean Excess Delay τ				RMS Delay Spread τ_{rms}			
	50 cm		1 m		50 cm		1 m	
	μ	σ	μ	σ	μ	σ	μ	σ
10 cm	33.53	1.24	36.09	0.80	20.05	2.24	21.94	2.32
20 cm	34.66	1.07	37.12	1.00	24.93	1.64	25.10	1.77
30 cm	35.87	0.72	37.55	0.65	24.84	2.17	25.34	3.41
40 cm	36.43	0.74	40.18	0.94	23.91	2.84	25.62	1.87

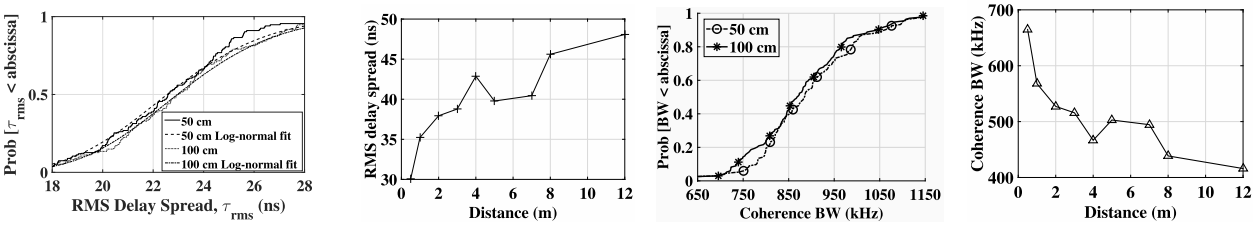

(a) (b) (c) (d)

Fig. 6. (a) Distribution of the RMS delay spread, $_{rms}$, for 50cm and 1m distance along with log-normal fit over all four depths in indoor testbed (silt loam) experiment, (b) The RMS delay spread, $_{rms}$, with distance in field (silty clay loam) experiment, (c) A distribution of coherence bandwidth for 50cm and 1m distance in indoor testbed (silt loam) experiment, (d) The coherence bandwidth with distance in field (silty clay loam) experiment.

communication distance is increased to 12m. The restriction placed on the coherence bandwidth by the increase in the RMS delay spread with distance and depth should be considered in system design, but a fine design line should not be drawn because of the additional impacts of soil moisture variations, as discussed next.

3) Soil Moisture Variations: In Fig. 7(a), the effect of soil moisture on amplitudes of delay profiles is shown for 50cm distance in indoor testbed (silt loam) experiment. Lower amplitudes can be observed for higher soil moisture (lower soil matric potential (cbar)), and this decrease is consistent over all delay ranges. The amplitude decrease varies between 5 8dB across the entire PDP.

Water in soil is classified into bound water and excess water. Water present in the first few particle layers of the soil is called bound water, firmly held by soil particles due to the effect of osmotic and matric forces [14]. Below these particle layers, the effects of osmotic and matric forces are reduced, which results in unrestricted water movement. However, the presence of salinity substantially changes the impact of osmotic potential (force) on soil-water movement dynamics. EM waves experience dispersion when interfaced with bound water. Since permittivity of soil varies with time due to variations in soil moisture, the wavelength in the soil also changes, which affects the wave attenuation.

In Fig. 7(b), the path loss with change in soil moisture (expressed as soil matric potential[4]) at 50cm and 1m distance and 10cm depth in indoor testbed (silt loam) experiment is shown. The path loss decreases by 3 4dB (7%) as soil matric

[4]Greater matric potential values indicate lower soil moisture and zero matric potential represents near saturation condition.

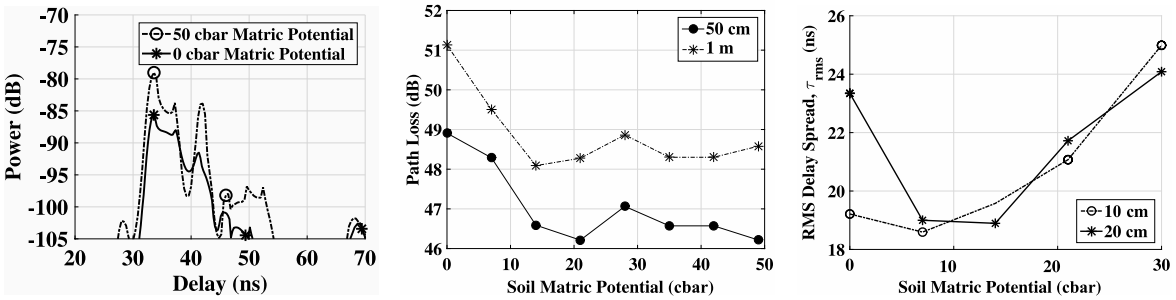

(a) (b) (c)

Fig. 7. Indoor testbed (silt loam) experiment: (a) Power delay profile, (b) Path loss with vs. soil moisture at 10 cm depth, (c) The RMS delay spread vs. soil moisture at $50\mathrm{cm}$ distance.

potential changes from $0\mathrm{to}\ 50\mathrm{cbar}$ (Centibars). In Fig. 7(c), RMS delay spread is shown as a function of soil moisture at $50\mathrm{cm}$ distance, for $10\mathrm{cm}$ and $20\mathrm{cm}$ depths in indoor testbed (silt loam) experiment. From near-saturation to $8\mathrm{cbar}$, the RMS delay spread decreases first and then, increases as soil moisture decreases. This can be attributed to a significantly reduced vertical infiltration rate at near saturation conditions. For $10\mathrm{cm}$ depth, the RMS delay spread increases from $19\mathrm{ns}$ to $25\mathrm{ns}$ (31%) as soil moisture decreases. Similar increase in the RMS delay spread with decrease in soil moisture can be observed for $20\mathrm{cm}$ depth. The low water absorption of EM waves with decrease in soil moisture contributes to increase in $_{\mathrm{rms}}$ as multipath components exhibit less attenuation.

The variations in amplitudes and path loss with the change in soil moisture lead to changes in coherence bandwidth, optimal system capacity, and communication coverage range. Specifically, an increase in the RMS delay spread with soil moisture decreases coherence bandwidth of the channel, and attenuation is also increased when soil moisture increases. Therefore, underground communication devices should have the ability to adjust their operation frequency, modulation scheme, and transmit power to compensate these changes caused by soil moisture variation [11]. Cognitive radio [4] solutions can be used to adopt parameters based on changing channel conditions.

4) Soil Type: Soils are divided into textural classes based on their particle size. To analyze soil texture effects, we have measured the channel statistics for silty clay loam, silt loam, and sandy soils. In Table IV, statistics of mean ( ) and standard deviation ( ) for the mean excess delay, the RMS delay spread and path loss for $50\mathrm{cm}$ and $1\mathrm{m}$ distances, and the four depths are shown.

The RMS delay spread $_{\mathrm{rms}}$ in sandy soil is $2\mathrm{ns}$ higher than that in silty clay loam, which is $1\mathrm{ns}$ higher than that in silt loam on average. Similarly, the path loss is $4\ \ 5\mathrm{dB}$ lower in sandy soil as compared to silt loam and silty clay loam. This is due to the lower attenuation in sandy soil. Attenuation of EM waves in the soil varies with soil type [10]. The soils containing the higher clay content suffer higher attenuation.

In sandy soil, there is a trade-off between attenuation and the RMS delay spread. The RMS delay spread $_{\mathrm{rms}}$ is large due to the least attenuated multipath components arriving at the receiver with considerable delays. On the other hand, overall attenuation is low as compared to silt loam and silty clay loam. Therefore, higher SNR can be achieved with moderate coherence bandwidth. Effects of soil texture must be taken into account during the design and deployment of WUSNs, and optimal system parameters such as communication range and data rates should be selected based on the physical characteristics of the soil.

5) Distance and Depth: The communication in UG channel is effected by depth and T-R separation. However, these impacts are much more severe than over the air communication. In Fig. 8(a), effects of T-R distance on PDP are shown in indoor testbed (silt loam) experiment. By increasing the distance from $50\mathrm{cm}$ to $1\mathrm{m}$, the first component in the $1\mathrm{m}$ PDP is delayed by $10\mathrm{ns}$. An $8\mathrm{dB}$ difference in peak amplitude is observed between profiles at $50\mathrm{cm}$ and $1\mathrm{m}$. Distribution of mean amplitudes of $50\mathrm{cm}$ and $1\mathrm{m}$ profiles at $40\mathrm{cm}$ depth in indoor testbed (silt loam) experiment is shown in Fig. 8(b). A $9\ \ 10\mathrm{dB}$ decrease in mean amplitude can be observed when T-R separation is increased from $50\mathrm{cm}$ to $1\mathrm{m}$. Peak amplitude of delay profile is decreased by $5\mathrm{dB}$ from $10\mathrm{cm}$ depth to $40\mathrm{cm}$ depth at $50\mathrm{cm}$ distance, whereas this decrease in peak amplitude is $20\mathrm{dB}$ for $1\mathrm{m}$ distance when depth is changed from $10\mathrm{cm}$ to $40\mathrm{cm}$. Since increase in burial depth increases the path of EM waves in soil, higher attenuation is observed.

EM waves in the soil are reflected and attenuated by the soil-air interface and suffer diffusion attenuation. The absorption of waves in the soil causes additional attenuation. Higher attenuation is the limiting factor for communication system design. The attenuation is increased with distance and depth because of the reflection effects of the lateral wave. At the soil-air interface, the phase of the lateral wave is randomly changed, which adds constructive-destructive interference at the receiver.

6) Operation Frequency: In Fig. 8(c), attenuation in dB is presented as a function of the operation frequency at different distances of up to $12\mathrm{m}$. Transmitter and receiver depths are set to $20\mathrm{cm}$. At $2\mathrm{m}$ distance, attenuation increases by $24\mathrm{dB}$ when frequency increases from $200\mathrm{MHz}$ to $400\mathrm{MHz}$. Similarly, for $200\mathrm{MHz}$, attenuation is increased from $51\mathrm{dB}$ to $92\mathrm{dB}$ (80%) when distance increases from $50\mathrm{cm}$ to $12\mathrm{m}$, leading to a $3\ 6\mathrm{dB}\ \mathrm{m}$ loss.

TABLE IV

MEAN ( ) AND STANDARD DEVIATION ( ) FOR THE MEAN EXCESS DELAY, THE RMS DELAY SPREAD AND PATH LOSS FOR 50cm AND 1m DISTANCES, AND 20cm DEPTH FOR THREE SOILS. VALUES ARE IN NANOSECONDS

Soil Type	Mean Excess Delay				RMS Delay Spread				Path Loss	
	Distance				Distance				Distance	
	50 cm		1 m		50 cm		1 m		50 cm	1 m
	μ	σ	μ	σ	μ	σ	μ	σ		
Silty Clay Loam	34.77	2.44	38.05	0.74	25.67	3.49	26.89	2.98	49 dB	52 dB
Silt Loam	34.66	1.07	37.12	1.00	24.93	1.64	25.10	1.77	48 dB	51 dB
Sandy Soil	34.13	1.90	37.87	0.80	27.89	2.76	29.54	1.66	40 dB	44 dB

TABLE V

SPEED OF THE WAVE IN ALL THREE SOILS, CALCULATED BY REFRACTIVE INDICES n BASED ON PARTICLE SIZE DISTRIBUTION OF SOILS GIVEN IN TABLE II

Soil Type	Speed in the Soil m/s	% of C	Refractive Index n
Silt Loam	$5.66\text{x}10^7$	18.89	5.28
Sandy Soil	$5.01\text{x}10^7$	16.71	5.98
Silty Clay Loam	$5.67\text{x}10^7$	18.91	5.29

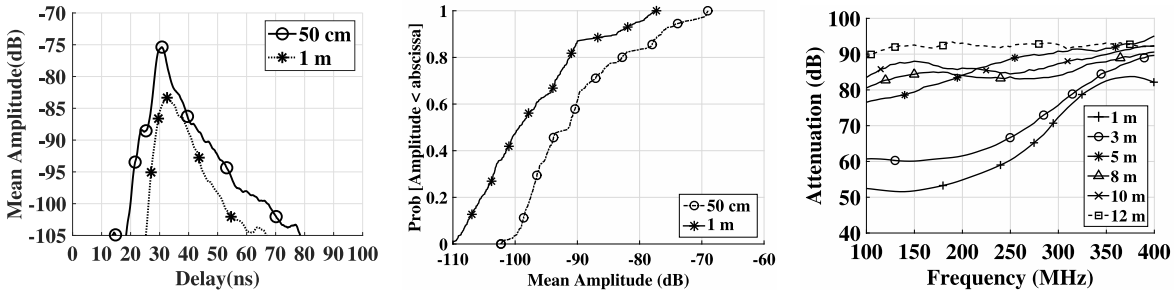

(a) (b) (c)

Fig. 8. Indoor testbed (silt loam) experiment: (a) Mean amplitudes of all 50cm and 1m profiles across all depths (b) Distribution function of mean amplitudes at 40cm depth. Field (silty clay loam) experiment: (c) Attenuation with frequency.

Higher frequencies suffer more attenuation because when EM waves propagate in the soil, their wavelength shortens due to higher permittivity of soil than the air. Hence, due to fewer effects of permittivity of soil on the lower frequency spectrum, it is more suitable for UG2UG communication as larger communication distances can be achieved. To have minimum attenuation, an operation frequency should be selected for each distance and depth such that attenuation is minimized. This is important from the WUSN topology design perspective because deployment needs to be customized to the soil type and frequency range of sensors being used for deployment. These results form the basis of the statistical model of the UG channel developed in Section. VII.

VII. STATISTICAL MODEL, EVALUATION AND EXPERIMENTAL VERIFICATION

To engineer an underground communication system, a statistical model of propagation in the wireless underground channel can help in optimizing system performance, designing tailored modulated/coding schemes, and in the end-to-end capacity analysis. For example, received data signals can be detected coherently in the absence of ISI. In this section, a detailed characterization of the underground channel is performed based on the measurements of Section VI. The multipath profiles taken in different soils under different soil moisture levels are analyzed to perform statistical analysis of the experimental data.

A. The Statistical Model

To model the wireless underground channel, our approach follows the standard OTA modeling approaches described in [16], [25], [34], and [42], with modifications due to the unique nature of wireless propagation in the UG channel. Based on the measurement analysis, the following assumptions are made:

1) The correlation among multipath components at different delays in the lateral, reflected, and direct components is very small and negligible for all practical purposes.

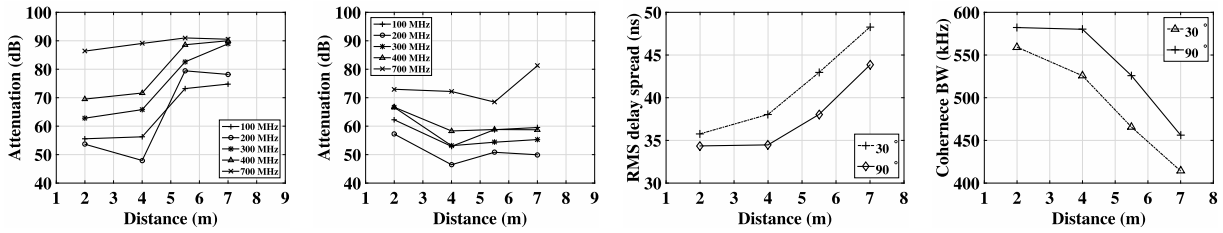

(a) (b) (c) (d)

Fig. 9. The attenuation with distance at different receiver angles (UG2AG): (a) 0 , (b) 90 , (c) The RMS delay spread with distance, (d) The coherence bandwidth with distance.

However, multipaths within each component are affected by the strongest path and hence, are correlated. Therefore, the tap-delay-lines are assumed uniformly spaced within each component.

2) At the receiver, phases are completely random with a uniform distribution over [0, 2).

To keep the model tractable, the arrival rate of delays within each component is kept constant, and amplitudes of these multipaths in each component are statistically independent. This helps in modeling the physical characteristics of the UG channel and provide ease of analysis without losing insight into delay statistics. The order of the arrival of the lateral, direct, and reflected components depends upon the burial depth, and distance between transmitter-receiver (T-R), because the path traversal through the soil and air exhibit different wave propagation speeds depending on the soil characteristics, and soil moisture level. Only for T-R distances less than 50cm, the direct component arrives first, and as the distance increases, the lateral component reaches the receiver first due to higher propagation speed in the air medium. Due to significant differences in the speed of the three components in soil and air mediums, no component overlap is observed, and the power of multipath components (gain) within each component decays before the arrival of the next component. Moreover, in our measurements, significant components were not observed beyond the 100ns time delay.

Next, statistics of amplitudes $_{l,i}$, $_{d,j}$, and $_{r,k}$ at delays $_{l,i}$, $_{d,j}$, and $_{r,k}$ for lateral, direct, and reflected waves, respectively, are derived. In Fig. 10, the mean amplitudes of a profile are shown at 50cm distance along with associated exponential decay fits. The analysis of the measurement data shows that gains of multipaths within each component follow exponential decay. Therefore, the path amplitudes of the three components are modeled as decaying exponentials within each component. Then, the multipath amplitudes are modeled as [34]:

$$_{l,i} = \ _{l0} e^{(\ _{l,i} \ \ _{l,0})\ _{L}} \quad 0 < i < L \tag{10}$$

$$_{d,j} = \ _{d0} e^{(\ _{d,j} \ \ _{d,0})\ _{D}} \quad 0 < j < D \tag{11}$$

$$_{r,k} = \ _{r0} e^{(\ _{r,k} \ \ _{r,0})\ _{R}} \quad 0 < k < R \tag{12}$$

where $_{l0}$, $_{d0}$, and $_{r0}$ are the gains of the first multipaths; $_{l0}$, $_{d0}$, and $_{r0}$ are the arrival times; $_{L}$, $_{D}$, and $_{R}$ are the decay rates; and L, D, and R are the number of multipaths for the lateral, direct, and reflected waves, respectively.

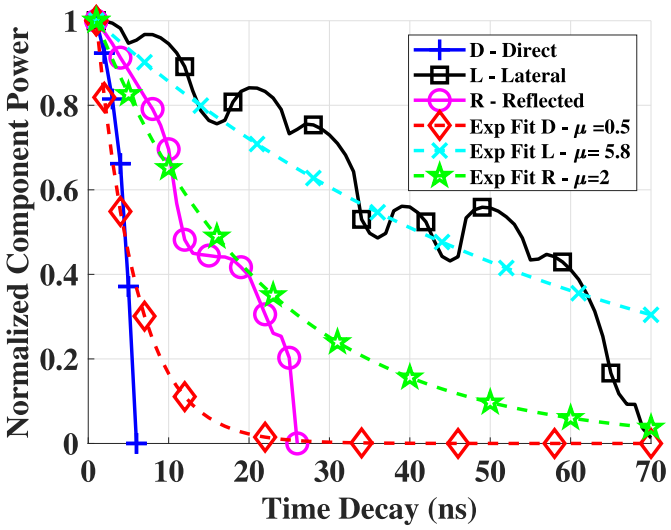

Fig. 10. The decay of three components with exponential decay fit.

The gains of the first multipaths are given as [12]:

$$\begin{aligned} _{l0} &= P_t + 20\log_{10}\ _{s} \quad 40\log_{10} d \quad 8.69\ _{s}(h_t + h_r) \\ &\quad +20\log_{10} T \quad 22 + 10\log_{10} D_{rl} \\ _{d0} &= P_t + 20\log_{10}\ _{s} \quad 20\log_{10} r_1 \quad 8.69\ _{s} r_1 \quad 22 \\ &\quad +10\log_{10} D_{rl} \\ _{r0} &= P_t + 20\log_{10}\ _{s} \quad 20\log_{10} r_2 \quad 8.69\ _{s} r_2 \\ &\quad +20\log_{10} \quad 22 + 10\log_{10} D_{rl} \end{aligned} \tag{13}$$

where P_t is the transmitted power, and T are reflection and transmission coefficients [12], respectively, r_2 is the length of the reflection path, $r_1 = \sqrt{(h_t \ \ h_r)^2 + d^2}$, $r_2 = \sqrt{(h_t + h_r)^2 + d^2}$, where h_t and h_r are transmitter and receiver burial depth, and $_s$ is the wavelength in soil [30].

In the statistical model, exponential decay is justified because the time delay depends on the travel paths, and the path gains are affected by the soil. Therefore, the gains of the successive multipaths depend on the delay of those multipaths. It is also important to note that, in addition to the soil moisture, the multipath gains $_{l,i}$, $_{d,j}$, and $_{r,k}$ are also impacted by soil type. For example, in sandy soils, path gains are much higher due to the lower attenuation as compared to the silt loam and silty clay loam soils due to the less water absorption of EM waves. This is attributed to the low water

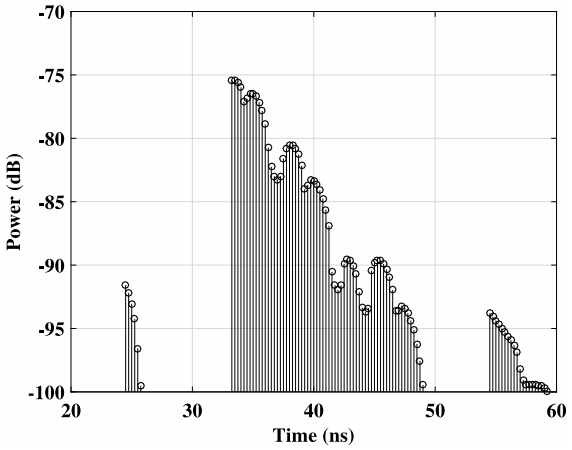

Fig. 11. A realization of wireless underground channel impulse response.

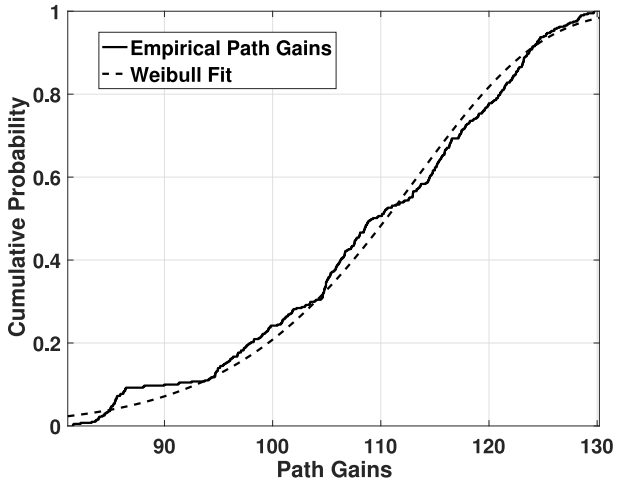

Fig. 12. Amplitude gains with Weibull distribution fit.

holding capacity of sandy soils. However, soil type impacts on multipaths gains $_{\mathrm{l},i}$, $_{\mathrm{d},j}$, and $_{\mathrm{r},k}$ do not require separate modeling in (10) - (12). Instead, this is captured in the first lateral, direct, and reflected components $_{\mathrm{l}\,0}$, $_{\mathrm{d}\,0}$, and $_{\mathrm{r}\,0}$ and are propagated to $_{\mathrm{l},i}$, $_{\mathrm{d},j}$, and $_{\mathrm{r},k}$ in (10) - (12).

Next, the number of significant paths are determined. The number of multipaths, L, D, and R, are determined by setting a gain threshold (paths within $30\mathrm{dB}$ from the peak). Multipath generation in a particular component is stopped once the path amplitude in that bin falls below the threshold value. This results in a larger number for sandy soil compared to those for silt loam and silty clay loam soils, which is also in good agreement with empirical observations. Moreover, this number is an indicator of the channel spread and depends on the soil moisture. The higher soil moisture leads to lower spread.

On the other hand, lower soil moisture decreases attenuation, which leads to the emergence of a larger number of multipaths falling above the threshold value and a larger number of multipaths. A realization of the underground channel impulse response model is shown in Fig. 11. The model parameters are shown in Table VI.

Up to this point, $_{\mathrm{l},i}$, $_{\mathrm{d},j}$, and $_{\mathrm{r},k}$ are calculated based on the delays within lateral, reflected, and direct components which depends on the exponential decay of multipath with respect to the main path gain in each component. This is a good realization of physical measurements. However, if we normalize the path gains of each components by the average of these gains such that $_{\mathrm{l},i}$ $_{\mathrm{l},i}$, $_{\mathrm{d},j}$ $_{\mathrm{d},j}$, and $_{\mathrm{r},k}$ $_{\mathrm{r},k}$, then, these amplitudes become independent of the delays, with which these are associated [34]. Accordingly, a commutative distribution of path gains normalized through this process is shown in Fig. 12, which follows the Weibull probability distribution.

B. Model Evaluations

The model parameters required to evaluate the statistical model are summarized in the Table VI. In the numerical evaluations, first, we need to find the the $_{\mathrm{l},i}$, $_{\mathrm{d},j}$, and $_{\mathrm{r},k}$ and their associated delays $_{\mathrm{l},i}$, $_{\mathrm{d},j}$, and $_{\mathrm{r},k}$. After generating the delays and amplitudes of these three components, other impulse response parameters are found and compared with the measurement data. An algorithm to generate UG channel impulse response is shown in Algorithm 1.

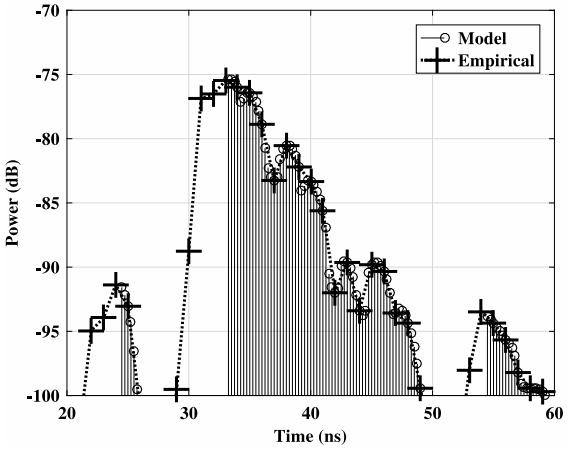

Fig. 13. Comparison of model and empirical impulse response in silt loam.

Algorithm 1 UG Channel Impulse Response Simulation

1: *Initialization*:
2: Input soil parameters
3: Obtain the soil moisture level
4: **BEGIN**
5: Generate the decay exponents for the lateral, direct, and reflected components
6: Determine the arrival time
7: Calculate the first multipath gain of each of the three components
8: Generate the multipaths and impulse response
9: **END**

The simulation algorithm takes soils parameters such as soil type and soil moisture as input, and calculates the arrival times of the lateral, direct, and reflected components, $_{\mathrm{l}\,0}$, $_{\mathrm{d}\,0}$, and

TABLE VI
THE IMPULSE RESPONSE MODEL PARAMETERS

Parameter	Description	Model	Values
S	Speed of wave in soil [32]	c/η	$\mathrm{c}= 3 \times 10^8$
η	Refraction Index [32]	$\eta = \sqrt{\sqrt{\epsilon'^2 + \epsilon''^2} + \epsilon'/2}$	ϵ', ϵ''
ϵ'	Real part of relative permittivity of the soil [23]	$\epsilon'_s = \begin{cases} 1.15\Big[1+\rho_b/\rho_s\left(\epsilon_s^{\delta}-1\right)+(m_v)^{\nu'}(\epsilon'_{fw})^{\delta}- \\ \quad m_v\Big]^{1/\delta} - 0.68 \qquad 0.3\,\mathrm{GHz} \le f \le 1.4\,\mathrm{GHz}\ , \\ \Big[1+\rho_b/\rho_s\left(\epsilon_s^{\delta}-1\right)+(m_v)^{\nu'}(\epsilon'_{fw})^{\delta}-m_v\Big]^{1/\delta} \\ \qquad\qquad 1.4\,\mathrm{GHz} \le f \le 18\,\mathrm{GHz}\ , \end{cases}$	S = Sand in %, C= Clay in %, $\delta = 0.65$, $\nu' = 1.2748 - 0.519S - 0.152C$, $\nu'' = 1.33797 - 0.603S - 0.166C$ ϵ'_{fw}, ϵ''_{fw}
ϵ''	Imaginary part of relative permittivity of the soil [23]	$\epsilon''_s = \Big[(m_v)^{\nu''}(\epsilon''_{fw})^{\delta},\Big]^{1/\delta}$	
ϵ'_{fw}	Real part of relative permittivity of the free water [23]	$\epsilon'_{fw} = e_{w\infty} + \frac{\epsilon_{w0}-\epsilon_{w\infty}}{1+(2\pi f\tau_w)^2}$	$\epsilon_{w\infty} = 4.9$ is the limit of ϵ'_{fw} when $f \to \infty$, ϵ_{w0} is the static dielectric constant for water, τ_w is the relaxation time for water, and ϵ_0 is the permittivity of free space. At room temperature, $2\pi\tau_w = 0.58 \times 10^{-10} s$ and $\epsilon_{w0} = 80.1$, effective conductivity, δ_{off}
ϵ''_{fw}	Imaginary part of relative permittivity of the free water [23]	$\epsilon''_{fw} = \frac{2\pi, f\tau_w(\epsilon_{w0}-\epsilon_{w\infty})}{1+(2\pi, f\tau_w)^2} + \frac{\delta_{eff}}{,2\pi\epsilon_0 f}\frac{(\rho_s-\rho_b)}{\rho_s m_v}$	
δ_{eff}	Effective conductivity of soil [23]	$\delta_{\text{eff}} = \begin{cases} 0.0467 + 0.2204\rho_b - 0.4111S + 0.6614C \\ \qquad\qquad 0.3\,\mathrm{GHz} \le f \le 1.4\,\mathrm{GHz}\ . \\ -1.645 + 1.939\rho_b - 2.25622S + 1.594C \\ \qquad\qquad 1.4\,\mathrm{GHz} \le f \le 18\,\mathrm{GHz} \end{cases}$	ρ_b is bulk density
$\tau_{\mathrm{l},0}$	Arrival time of lateral component	$\tau_{\mathrm{l}} = 2 \times (\delta_{\mathrm{s}}/S) + (\delta_{\mathrm{a}}/c)$	S is speed of wave in soil c is speed of wave in air
$\tau_{\mathrm{d},0}$	Arrival time of direct component	$\tau_{\mathrm{d}} = (\delta_{\mathrm{s}}/S)$	S is speed of wave in soil
$\tau_{\mathrm{r},0}$	Arrival time of reflected component	$\tau_r = 2 \times (\delta_{\mathrm{s}}/S)$	S is speed of wave in soil
$\alpha_{\mathrm{l},0}$, $\alpha_{\mathrm{d},0}$, $\alpha_{\mathrm{r},0}$,	Gains of the three main components	$\alpha_{\mathrm{l},0} = P_{\mathrm{t}} + 20\log_{10}\lambda_{\mathrm{s}} - 40\log_{10} d - 8.69\alpha_{\mathrm{s}}(h_{\mathrm{t}} + h_{\mathrm{r}})$ $+20\log_{10} T - 22 + 10\log_{10} D_{\mathrm{rl}}$, $\alpha_{\mathrm{d},0} = P_{\mathrm{t}} + 20\log_{10}\lambda_{\mathrm{s}} - 20\log_{10} r_1 - 8.69\alpha_{\mathrm{s}} r_1$ $-22 + 10\log_{10} D_{\mathrm{rl}}$ $\alpha_{\mathrm{r},0} = P_{\mathrm{t}} + 20\log_{10}\lambda_{\mathrm{s}} - 20\log_{10} r_2 - 8.69\alpha_{\mathrm{s}} r_2$ $+20\log_{10}\Gamma - 22 + 10\log_{10} D_{\mathrm{rl}}$	μ and σ
$\alpha_{\mathrm{l},i}$, $\alpha_{\mathrm{d},j}$, $\alpha_{\mathrm{r},k}$	Path amplitudes of the three components	$\alpha_{\mathrm{l},i} = \alpha_{\mathrm{l},0} e^{-(\tau_{\mathrm{l},i}-\tau_{\mathrm{l},0})/\gamma_L}\ \forall,\ 0 < i < L$ $\alpha_{\mathrm{d},j} = \alpha_{\mathrm{d},0} e^{-(\tau_{\mathrm{d},j}-\tau_{\mathrm{d},0})/\gamma_D}\ \forall,\ 0 < j < D$ $\alpha_{\mathrm{r},k} = \alpha_{\mathrm{r},0} e^{-(\tau_{\mathrm{r},k}-\tau_{\mathrm{r},0})/\gamma_R}\ \forall,\ 0 < k < R$	

$\tau_{\mathrm{r},0}$. Based on the soil type, peak power gains $\alpha_{\mathrm{l},0}$, $\alpha_{\mathrm{d},0}$, and $\alpha_{\mathrm{r},0}$ are determined from the Table VI. The model parameters for peak amplitude, delays, and number of multipaths statistics for lateral, direct, and reflected components for three soil types are given in [32, Table VI].

The different statistical parameters computed from the measurement data and the channel model numerical evaluations are compared in Table VII. UG channel is evaluated numerically using the the statistical model. The RMS delay spread and the coherence bandwidth parameters are derived and compared with the parameters obtained through empirical data. Model prediction errors for the RMS delay spread and coherence bandwidth are 14.67% and 14.08%, respectively. It can be observed that the difference in predicted and measured values, which is due to model uncertainty and observational error,

TABLE VII
THE VALIDATION OF IMPULSE RESPONSE MODEL PARAMETERS

Impulse Response Parameter	Measured	Modeled
RMS Delay Spread (τ_{rms})	$45.52\,\mathrm{ns}$	$38.84\,\mathrm{ns}$
Coherence Bandwidth	$439\,\mathrm{kHz}$	$514\,\mathrm{kHz}$

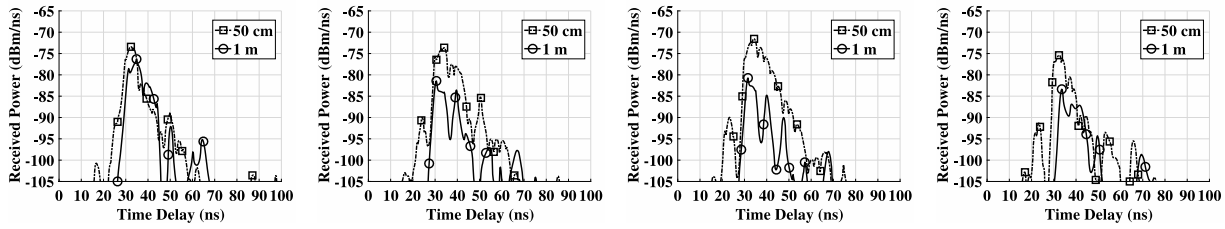

(a) 10 cm (b) 20 cm (c) 30 cm (d) 40 cm

Fig. 14. Power Delay Profiles (PDP) measured at 50cm and 1m distance, at different depths in silt loam soil at near-saturation: (a) 10cm, (b) 20cm, (c) 30cm, (d) 40cm.

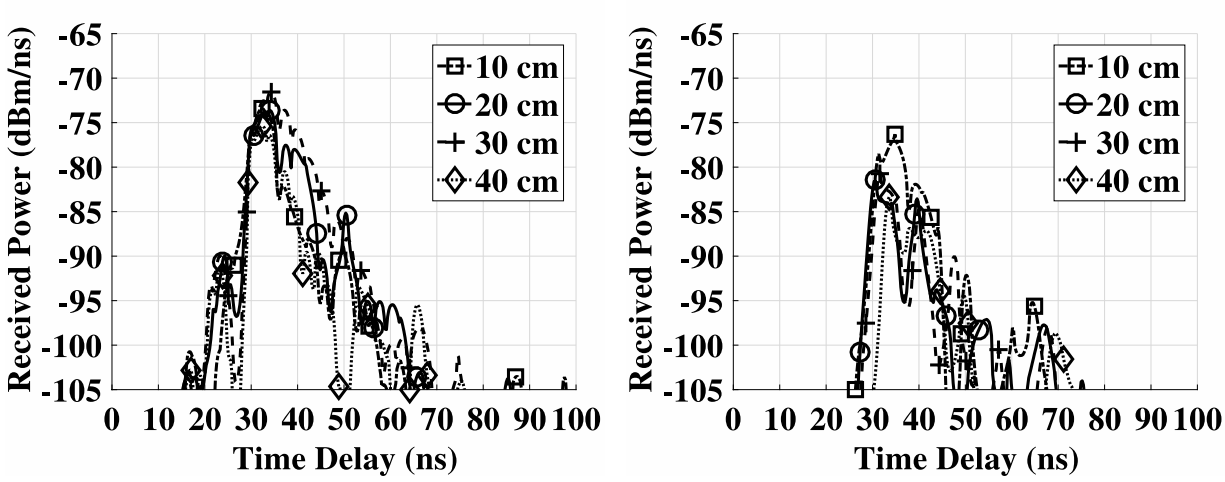

(a) 50 cm (b) 1 m

Fig. 15. The power delay profile in silt loam soil at different depths at: (a) 50cm T-R distance, (b) 1m T-R distance.

is less than 15%. Overall, the developed statistical model shows a good agreement with the empirical data, and statistics of the coherence bandwidth and the RMS delay spread prove the validity of the statistical model.

C. Empirical Validation

A good statistical model should be able to simulate the empirical measurements with high accuracy. Moreover, the simulated response must have the same characteristics as the measurement results. In this section, the arrival of multipath components is validated with experiments conducted in the indoor testbed. Moreover, the shape of the PDP is presented, and physical interpretations are discussed.

The speed of the wave in all three soils is found by calculating the refractive indices n based on particle size distribution and classification of soils given in Table I. The results of these calculations are shown in Table V. In Fig. 13, a measured PDP for a silt loam at 40cm depth is compared with a schematic representation of the 3-wave model for T-R separation of 50cm. Analysis of arrival time of three components reveals that for 50cm distance and all burial depths, lateral waves arrive later than the direct waves except for the 10cm depth where lateral waves reach the receiver first. It can be observed that measurement data shows a strong agreement with the model.

In Fig. 13, it can also be observed that the lateral component is the strongest compared to the direct and reflected components. This is because direct and reflected components are spherical waves, propagating radially outward from the antenna, whereas, the lateral component is, initially, a plane wave that travels upward from the source to the boundary, then horizontally as a cylindrical wave, and subsequently travels backward as a plane wave from the boundary to the point of observation. The proposed model applies to different environments for underground wireless communications. Accordingly, tailored sensing, control, and communication strategies can be developed.

VIII. The Power Delay Profile Measurements

In this section, we present the underground channel impulse response measurements. In Fig. 14, PDPs of 50cm and 1m distances are compared for all depths. The first multipath component in the PDPs is the direct wave component, which is present at 18 28ns for the 50cm profile, and it is not observed for the 1m profile. This is because direct wave suffers less attenuation at a distance of 50cm than 1m. It is observed that the lateral wave component is the strongest in all power delay profiles and is formed at 30 40ns. The delays of the lateral wave for both 50cm and 1m profiles are similar because the wave propagates much faster in the air than in soil. In general,

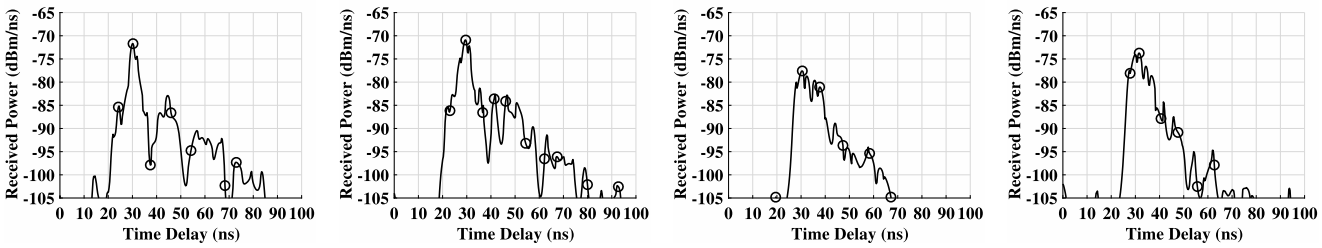

(a) 0 cbar (wet)-50 cm (b) 50 cbar (dry)-50 cm (c) 0 cbar (wet)-1 m (d) 50 cbar (dry)-1 m

Fig. 16. Power Delay Profiles (PDP) measured at 50cm and 1m distance, at 20cm depths for different soil moisture levels: (a) 0cbar-50cm, (b) 50cbar-50cm, (c) 0cbar-1m, (d) 50cbar-1m.

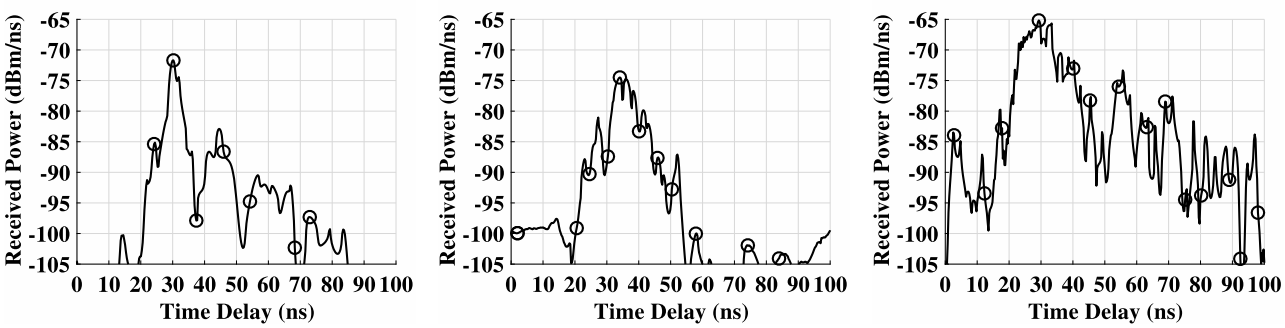

(a) Silt Loam (b) Silty Clay Loam (c) Sandy Soil

Fig. 17. The Power Delay Profiles (PDP) measured in different soils: (a) Silt Loam, (b) Silty Clay Loam, (c) Sandy Soil.

the lateral wave component is 10dB to 15dB higher in power than the direct wave component.

In Figs. 15, PDPs of the communication channels at four depths are shown for T-R distances of 50cm (Fig. 15(a)) and 1m (Fig. 15(b)). At the same distance, with the increase in depth, the received power of lateral wave decreases. This is more significant in the 1m case, where the peak power of the lateral wave is -75dB for the depth of 10cm, while it is -83dB when the depth increases to 40cm. Also shown in Fig. 15(b), with an increase in depth, the component delay also increases. At 10cm depth, the lateral wave arrives at 29ns while at 40cm it arrives at 32ns. Distance related delay of $10-15$ns can also be observed in all profiles by comparing distances of 50cm and 1m distances.

In Figs. 16, PDP measured at T-R distances of 50cm and 1m, at the 20cm depth for soil moisture levels of 0cbar (wet) and 50cbar (dry) are shown. For the T-R distance of 50cm, it can be observed that a decrease in soil moisture leads to larger received power for multi-path components. Similar observations are made for the T-R distance of 1m. It is also important to note that direct component vanishes as distance increases, which is caused by the higher attenuation in the soil. Finally, in Fig. 17, the measured PDPs in different soils are shown. It can be observed that due to the low water holding capacity of the sandy soil, it has a higher received power across all three components (Fig. 17(c)) as compared to the silt loam (Fig. 17(a)) and silty clay loam soil (Fig. 17(b)).

IX. Conclusion

In this article, the analysis of the impulse response of the wireless underground channel is presented. A 3-wave-based impulse response model of the underground channel is developed and validated with measured data. Distribution of mean excess delay and the RMS delay spread is determined, and it is shown that the RMS delay spread is log-normally distributed. The effect of T-R separation on the mean amplitudes of the power delay profile is shown. We have presented the impact of soil moisture and soil types on the RMS delay spread and power gains of delay profiles. It is presented that the RMS delay spread increases with an increase in soil moisture. It is also showed that coarse-textured soils have larger the RMS delay spreads and lower attenuation as compared to fine and medium-textured soils. Based on the RMS delay spread, the UG channel's coherence bandwidth is modeled and shown to be less than 1MHz. Coherence bandwidth findings reveled the use of OFDM for underground channel communication to have ISI free communication and for significant performance improvements. These findings serve as important characterization parameters of the UG channel and give guidelines for the design of an underground communication system.

References

[1] P. Abouzar, D. G. Michelson, and M. Hamdi, "RSSI-based distributed self-localization for wireless sensor networks used in precision agriculture," *IEEE Trans. Wireless Commun.*, vol. 15, no. 10, pp. 6638–6650, Oct. 2016.

[2] T. E. Abrudan, O. Kypris, N. Trigoni, and A. Markham, "Impact of rocks and minerals on underground magneto-inductive communication and localization," *IEEE Access*, vol. 4, pp. 3999–4010, 2016.

[3] M. A. Akkaş, "Channel modeling of wireless sensor networks in oil," *Wireless Pers. Commun.*, vol. 95, pp. 4337–4355, Mar. 2017, doi: 10.1007/s11277-017-4083-9.

[4] I. F. Akyildiz, W.-Y. Lee, M. C. Vuran, and S. Mohanty, "NeXt generation/dynamic spectrum access/cognitive radio wireless networks: A survey," *Comput. Netw.*, vol. 50, no. 13, pp. 2127–2159, Sep. 2006.

[5] I. F. Akyildiz, Z. Sun, and M. C. Vuran, "Signal propagation techniques for wireless underground communication networks," *Phys. Commun.*, vol. 2, no. 3, pp. 167–183, Sep. 2009.
[6] A. O. Bicen, A. B. Sahin, and O. B. Akan, "Spectrum-aware underwater networks: Cognitive acoustic communications," *IEEE Veh. Technol. Mag.*, vol. 7, no. 2, pp. 34–40, Jun. 2012.
[7] H. R. Bogena, J. A. Huisman, H. Meier, U. Rosenbaum, and A. Weuthen, "Hybrid wireless underground sensor networks: Quantification of signal attenuation in soil," *Vadose Zone J.*, vol. 8, no. 3, pp. 755–761, Aug. 2009.
[8] H. R. Bogena, M. Herbst, J. A. Huisman, U. Rosenbaum, A. Weuthen, and H. Vereecken, "Potential of wireless sensor networks for measuring soil water content variability," *Vadose Zone J.*, vol. 9, no. 4, pp. 1002–1013, Nov. 2010.
[9] D. Cassioli, M. Z. Win, and A. F. Molisch, "The ultra-wide bandwidth indoor channel: From statistical model to simulations," *IEEE J. Sel. Areas Commun.*, vol. 20, no. 6, pp. 1247–1257, Aug. 2002.
[10] M. Dobson, F. Ulaby, M. Hallikainen, and M. El-rayes, "Microwave dielectric behavior of wet soil-part II: Dielectric mixing models," *IEEE Trans. Geosci. Remote Sens.*, vols. GE–23, no. 1, pp. 35–46, Jan. 1985.
[11] X. Dong and M. C. Vuran, "Impacts of soil moisture on cognitive radio underground networks," in *Proc. 1st Int. Black Sea Conf. Commun. Netw. (BlackSeaCom)*, Jul. 2013, pp. 222–227.
[12] X. Dong and M. C. Vuran, "A channel model for wireless underground sensor networks using lateral waves," in *Proc. IEEE Global Telecommun. Conf. (GLOBECOM)*, Houston, TX, USA, Dec. 2011, pp. 1–6.
[13] X. Dong, M. C. Vuran, and S. Irmak, "Autonomous precision agriculture through integration of wireless underground sensor networks with center pivot irrigation systems," *Ad Hoc Netw.*, vol. 11, no. 7, pp. 1975–1987, 2013.
[14] H. D. Foth, *Fundamentals of Soil Science*, 8th ed. Hoboken, NJ, USA: Wiley, 1990.
[15] H. Guo and Z. Sun, "Channel and energy modeling for self-contained wireless sensor networks in oil reservoirs," *IEEE Trans. Wireless Commun.*, vol. 13, no. 4, pp. 2258–2269, Apr. 2014.
[16] H. Hashemi, "Impulse response modeling of indoor radio propagation channels," *IEEE J. Sel. Areas Commun.*, vol. 11, no. 7, pp. 967–978, Sep. 1993.
[17] S. J. Howard and K. Pahlavan, "Measurement and analysis of the indoor radio channel in the frequency domain," *IEEE Trans. Instrum. Meas.*, vol. 39, no. 5, pp. 751–755, Oct. 1990.
[18] S. Irmak and D. Haman, "Performance of the watermark. Granular matri x sensor in sandy soils," *Appl. Eng. Agricult.*, vol. 17, no. 6, pp. 787–795, 2001.
[19] S. Irmak and A. Irmak, "Performance of frequency-domain reflectometer, capacitance, and psuedo-transit time-based soil water content probes in four coarse-textured soils," *Appl. Eng. Agricult.*, vol. 21, no. 6, pp. 999–1008, 2005.
[20] M. N. Islam, B.-J.-J. Kim, P. Henry, and E. Rozner, "A wireless channel sounding system for rapid propagation measurements," in *Proc. IEEE Int. Conf. Commun. (ICC)*, Jun. 2013, pp. 5720–5725.
[21] R. W. P. King, M. Owens, and T. T. Wu, *Lateral Electromagnetic Waves*. New York, NY, USA: Springer-Verlag, May 1992.
[22] S.-C. Lin, I. F. Akyildiz, P. Wang, and Z. Sun, "Distributed cross-layer protocol design for magnetic induction communication in wireless underground sensor networks," *IEEE Trans. Wireless Commun.*, vol. 14, no. 7, pp. 4006–4019, Jul. 2015.
[23] N. R. Peplinski, F. T. Ulaby, and M. C. Dobson, "Dielectric properties of soil in the 0.3–1.3 GHz range," *IEEE Trans. Geosci. Remote Sens.*, vol. 33, no. 3, pp. 803–807, May 1995.
[24] M. A. Poletti, "The application of linearly swept frequency measurements," *J. Acoust. Soc. Amer.*, vol. 84, no. 2, pp. 599–610, Aug. 1988.
[25] T. S. Rappaport, S. Y. Seidel, and K. Takamizawa, "Statistical channel impulse response models for factory and open plan building radio communicate system design," *IEEE Trans. Commun.*, vol. 39, no. 5, pp. 794–807, May 1991.
[26] A. Salam and M. C. Vuran, "Impacts of soil type and moisture on the capacity of multi-carrier modulation in Internet of underground things," in *Proc. 25th Int. Conf. Comput. Commun. Netw. (ICCCN)*, Waikoloa, HI, USA, Aug. 2016, pp. 1–9.
[27] A. Salam and M. C. Vuran, "Smart underground antenna arrays: A soil moisture adaptive beamforming approach," in *Proc. IEEE Conf. Comput. Commun. (INFOCOM)*, Atlanta, GA, USA, May 2017, pp. 1–9.
[28] A. Salam, M. C. Vuran, X. Dong, C. Argyropoulos, and S. Irmak, "A theoretical model of underground dipole antennas for communications in Internet of underground things," *IEEE Trans. Antennas Propag.*, vol. 67, no. 6, pp. 3996–4009, Jun. 2019.
[29] A. Salam, M. C. Vuran, and S. Irmak, "Di-sense: *In situ* real-time permittivity estimation and soil moisture sensing using wireless underground communications," *Comput. Netw.*, vol. 151, pp. 31–41, Mar. 2019. [Online]. Available: http://www.sciencedirect.com/science/article/pii/S1389128618303141
[30] A. Salam and M. C. Vuran, "Smart underground antenna arrays: A soil moisture adaptive beamforming approach," Dept. Comput. Sci. Eng., Univ. Nebraska-Lincoln, Lincoln, Nebraska, Tech. Rep. TR-UNL-CSE-2017-0001, Jan. 2017.
[31] A. Salam and M. C. Vuran, "Wireless underground channel diversity reception with multiple antennas for Internet of underground things," in *Proc. IEEE Int. Conf. Commun. (ICC)*, Paris, France, May 2017, pp. 1–7.
[32] A. Salam, M. C. Vuran, and S. Irmak, "Pulses in the sand: Impulse response analysis of wireless underground channel," in *Proc. 35th Annu. IEEE Int. Conf. Comput. Commun. (INFOCOM)*, San Francisco, CA, USA, Apr. 2016, pp. 1–9.
[33] A. Salam, M. C. Vuran, and S. Irmak, "Towards Internet of underground things in smart lighting: A statistical model of wireless underground channel," in *Proc. IEEE 14th Int. Conf. Netw., Sens. Control (ICNSC)*, Calabria, Italy, May 2017, pp. 574–579.
[34] A. A. M. Saleh and R. Valenzuela, "A statistical model for indoor multipath propagation," *IEEE J. Sel. Areas Commun.*, vol. 5, no. 2, pp. 128–137, Feb. 1987.
[35] A. M. Street, L. Lukama, and D. J. Edwards, "Use of VNAs for wideband propagation measurements," *IEE Proc.-Commun.*, vol. 148, no. 6, pp. 411–415, Dec. 2001.
[36] Z. Sun and I. Akyildiz, "Channel modeling and analysis for wireless networks in underground mines and road tunnels," *IEEE Trans. Commun.*, vol. 58, no. 6, pp. 1758–1768, Jun. 2010.
[37] X. Tan, Z. Sun, and I. F. Akyildiz, "Wireless Underground Sensor Networks: MI-based communication systems for underground applications," *IEEE Antennas Propag. Mag.*, vol. 57, no. 4, pp. 74–87, Aug. 2015.
[38] M. J. Tiusanen, "Wideband antenna for underground soil scout transmission," *IEEE Antennas Wireless Propag. Lett.*, vol. 5, pp. 517–519, 2006.
[39] F. T. Ulaby and D. G. Long, *Microwave Radar and Radiometric Remote Sensing*. Ann Arbor, MI, USA: Univ. Michigan Press, 2014.
[40] M. C. Vuran and I. F. Akyildiz, "Channel model and analysis for wireless underground sensor networks in soil medium," *Phys. Commun.*, vol. 3, no. 4, pp. 245–254, Dec. 2010.
[41] M. C. Vuran, A. Salam, R. Wong, and S. Irmak, "Internet of underground things in precision agriculture: Architecture and technology aspects," *Ad Hoc Netw.*, vol. 81, pp. 160–173, Dec. 2018.
[42] M. Z. Win and R. A. Scholtz, "Characterization of ultra-wide bandwidth wireless indoor channels: A communication-theoretic view," *IEEE J. Sel. Areas Commun.*, vol. 20, no. 9, pp. 1613–1627, Dec. 2002.

Abdul Salam (Member, IEEE) received the B.Sc. and M.S. degrees in computer science from Bahauddin Zakariya University, Multan, Pakistan, in 2001 and 2004, respectively, the M.S. degree in computer engineering from UET, Taxila, Pakistan, in 2012, and the Ph.D. degree in computer engineering from the Department of Computer Science and Engineering, University of Nebraska–Lincoln, Lincoln, NE, USA. He was a Lecturer with the Department of Computer Science, Bahauddin Zakariya University, and the Department of Computer Science and Information Technology, Islamia University, Bahawalpur, Pakistan. He is currently an Assistant Professor with the Department of Computer and Information Technology, Purdue University, West Lafayette, IN, USA. He is the author of the book *Internet of Things for Sustainable Community Development*. His current research interests include sustainability, wireless networking, digital agriculture, and the Internet of Things.

Mehmet C. Vuran (Member, IEEE) received the B.Sc. degree in electrical and electronics engineering from Bilkent University, Ankara, Turkey, in 2002, and the M.S. and Ph.D. degrees in electrical and computer engineering from the Georgia Institute of Technology, Atlanta, in 2004 and 2007, respectively, under the guidance of Prof. Ian F. Akyildiz. He is currently the Susan J. Rosowski Professor of computer science and engineering with the University of Nebraska–Lincoln and the Robert B. Daugherty Water for Food Institute Fellow. His current research interests include wireless underground communications, cognitive radio networks, cross-layer design, and correlation-based communication. He was recognized as the Thomson Reuters/Clarivate Analytics Highly Cited Researcher in computer science in 2014, 2015, and 2016. He was a recipient of the NSF CAREER Award in 2010 and the coauthor of *Wireless Sensor Networks* textbook. He is an Associate Editor of the IEEE COMMUNICATIONS SURVEYS AND TUTORIALS, the IEEE TRANSACTIONS ON MOBILE COMPUTING, and the IEEE TRANSACTIONS ON NETWORK SCIENCE AND ENGINEERING.

Suat Irmak received the Ph.D. degree in agricultural and biological engineering with the emphasis on land and soil-water resources and irrigation engineering from the University of Florida. He is currently the Harold W. Eberhard Distinguished Professor with the Department of Biological Systems Engineering, University of Nebraska–Lincoln. In addition, he has Courtesy Full Professor appointments with the Department of Earth and Atmospheric Sciences and the Department of Agronomy and Horticulture. He holds numerous leadership roles at the American Society of Civil Engineers-Environmental and Water Resources Institute, for which he chairs the Evapotranspiration in Irrigation Hydrology Committee, the American Society of Agricultural and Biological Engineers (ASABE), and the United States Committee on Irrigation and Drainage. He has earned numerous awards and honors, including the ASABE John Deere Gold Medal Award, the Heermann Sprinkler Irrigation Award, the New Holland Young Researcher Award, and the ASABE Young Extension Professional Award. His research interests include extension and educational programs apply engineering and scientific fundamentals in soil and water resources engineering, irrigation engineering and agricultural water management, crop water productivity, evapotranspiration and other surface energy fluxes for agro-ecosystems, invasive plant species water use, and impacts of changes in climate variables on water resources and agro-ecosystem productivity. He leads the Nebraska Agricultural Water Management Network, which aims to increase adoption of new tools, technologies (including advanced soil moisture sensing devices) and strategies for increasing crop water productivity and reducing energy use in agriculture. He has established the Nebraska Water and Energy Flux Measurement, Modeling and Research Network, made up of 12 water and surface energy flux towers forming a comprehensive network that measures surface energy and water vapor fluxes, microclimatic variables, plant physiological parameters and biophysical properties, water use efficiency, soil water content, and surface characteristics and their interactions for various agro-ecosystems.